Orientationally ordered states of a wormlike chain in spherical confinement

Qin Liang,[1,2,*] Ying Jiang,[2] and Jeff Z. Y. Chen [3,†]

[1]*Faculty of Mathematics and Computational Science, Xiangtan University, Xiangtan, Hunan 411105, China*
[2]*School of Chemistry, Beihang University, Beijing 100191, China*
[3]*Department of Physics and Astronomy, University of Waterloo, Waterloo, Ontario, Canada N2L 3G1*

One of the basic characteristics of a linear dsDNA molecule is its persistence length, typically of order 50 nm. The DNA chain inflicts a large energy penalty if it is bent sharply at that length scale. Viruses of bacteria, known as bacteriophages, typically have a dimension of a few tens of nanometers. Yet, it is known that a bacteriophage actively packages viral DNA inside the capsid and ejects it afterwards. Here, adopting a commonly used polymer model known as the wormlike chain, we answer an idealized question: Placing a linear DNA molecule inside a spherical cavity, what ordered states can we derive from known tools in statistical physics? Solving the model in a rigorous field-theory framework, we report a universal phase diagram for four orientationally ordered and disordered states, in terms of two relevant physical parameters.

I. INTRODUCTION

The issue of the packing structures of a dsDNA molecule inside a confinement cage is a half-century-old problem. Extensive experimental efforts have been devoted to the subject, particularly on DNA inside bacteriophage capsids [1–15]. The Particle-based computer simulations of coarse-grained models, which model DNA by a self-avoiding semiflexible polymer chain in confinement of cavities of simply spherical or more realistic shapes, have also enlightened us with the possible packing structures [16–25]. The main driving force is the intrachain excluded-volume interactions, after the DNA winds around inside the capsid, which prefers DNA strands to locally align in parallel. The commonly acknowledged physical picture is that the linear molecule winds into a spool [1–23,26–28], but variations of the spooling details exist in the literature.

Complementary to experimental methods and particle-based computer simulations, a theoretical analysis of the subject, which is usually further aided by numerical computations, provides a different perspective but is rarer. As far as we know, the only existing theoretical study is based on the Frank model, which treats the overall DNA texture as a nematic field, with three phenomenological distortion-energy penalties as the system parameters [29]. Our aim in this paper is to clearly present a unified view of the ordered and disordered states, as a function of physically tractable parameters such as confined DNA length and excluded-volume diameter, on the basis of solving the free-energy problem of the wormlike-chain model confined in a spherical cavity.

The theoretical model here assumes that the DNA molecule is a semiflexible polymer of thickness diameter d, total contour length L, and persistence length P, such that $d/P \ll 1$

and $L/P \gg 1$. In total, n polymer chains (for most DNA-confinement problems, $n = 1$) are completely placed inside a spherical cavity of radius R and interact with the confinement wall by a steric repulsion only. The P/R ratio is a system parameter here that controls the strength of confinement, from strong (large P/R) to weak (small P/R). The predominant segment-segment interactions between DNA strands that drive the orientational ordering are formulated in terms of the second-virial free-energy term, originally proposed by Onsager [30].

Hypothetically, if we could ignore the chain connectivity for a moment, the system would effectively contain $n_{\mathrm{eff}} = nL/P$ rodlike segments confined inside a volume $V = 4\pi R^3/3$; according to Onsager, the lyotropic liquid-crystal phase transition takes place when the average relative rod density $\rho_0 = 2n_{\mathrm{eff}} P^2 d/V$, or

$$\rho_0 = \frac{3}{2\pi} \frac{d}{P} \left(\frac{P}{R}\right)^3 \frac{nL}{P}, \tag{1}$$

reaches a critical value. Quantitatively, we can show that the self-consistent field theory (SCFT, outlined in Appendix A) gives rise to the same ρ_0 as the basic parameter for a long, wormlike, and *connected* polymer in spherical confinement, independent of the above rough estimate. In physical units, this density regime corresponds to $n_{\mathrm{eff}}/V \sim 1/(P^2 d)$, which is much less than the close packing density $n_{\mathrm{eff}}/V \sim 1/(Pd^2)$.

Hence, en route to close packing which happens at a much higher density, one expects liquid-crystal-type phase transitions in confined DNA. The most important physical property of the current system is the connection between the polymer segments which strongly couples density inhomogeneity and orientational ordering; once this coupling is correctly installed in our theory, instead of the liquid-crystal transition, we find transitions to three spooling states: coaxial spool (CS) as commonly acknowledged on this topic, Hopf fibration (HF), and condensed HF (CHF). All are illustrated in Fig. 1 and discussed in Sec. II. The evidences of the coexistence of two

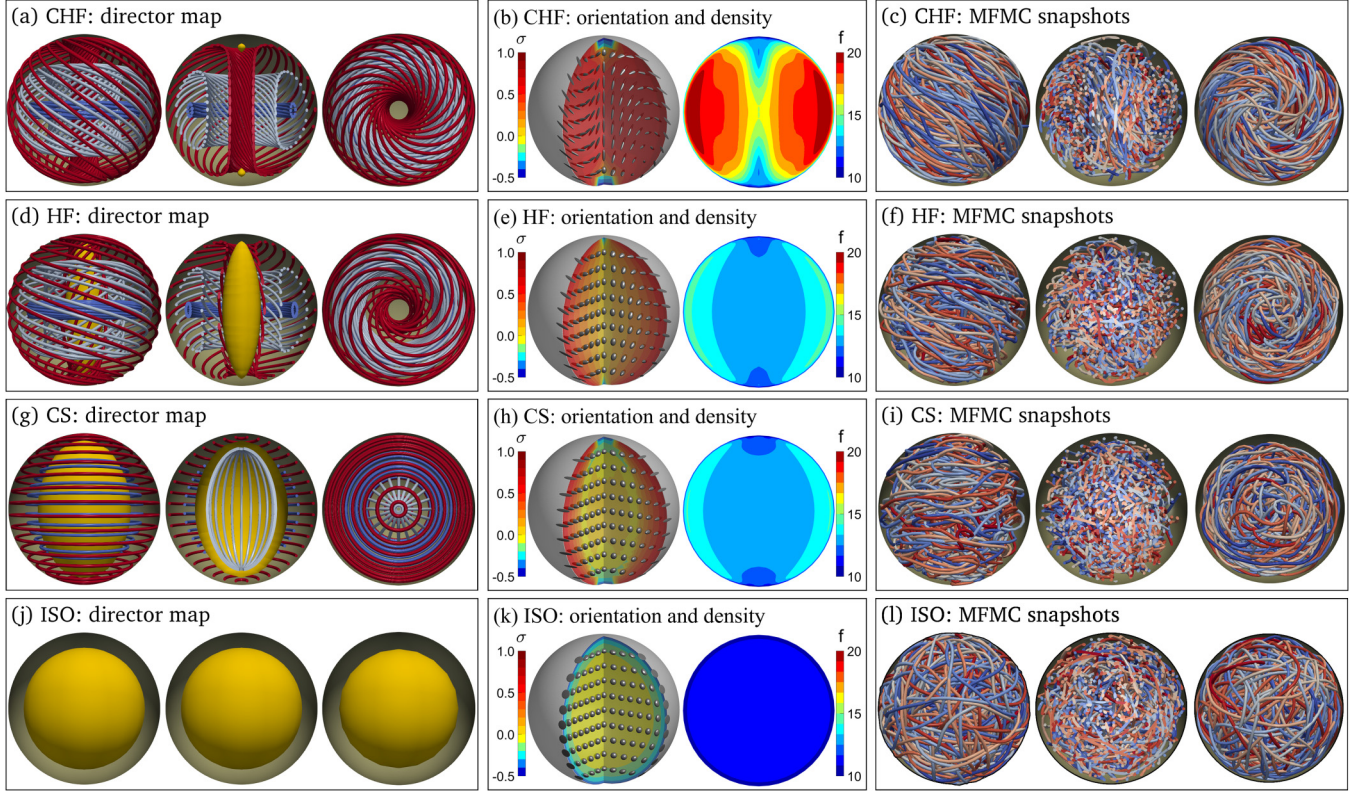*liangqin1997@xtu.edu.cn
†jeffchen@uwaterloo.ca

FIG. 1. Structural illustrations of the four states, CHF, HF, CS, and ISO, found from SCFT. The director maps in (a), (d), and (g) are drawn by connecting the local long-axis nematic directions. On the basis of using the symmetry axis as the south-north pole axis, the left panels of (a), (d), (g), and (j) are side views, the middle panels cross-section views, and the right panels top views from the north pole. Three sets of director lines are shown: red, light grey, and light blue. The yellow region is the isotropic core ($|\sigma| \sim 0$). In (g), the nematic directors shown by light grey lines form a weak splay pattern. The left panels of (b), (e), (h), and (k) are plots of the local orientational distribution represented by ellipsoids. The needlelike and pancakelike shapes indicate local nematic ordering with positive and negative long-axis order parameter σ; a spherical shape indicates isotropic ordering with $\sigma = 0$. The local density is shown in the right panels. The side (left), cross-section (middle), and top views (right) of (c), (f), (i), and (l) were produced according to the actual chain coordinates taken from mean-field Monte Carlo (MFMC) simulations, where colors have no particular meanings. All graphs in this figure were produced by taking parameters $[\rho_0, P/R] = [18, 1]$ (CHF), [13.56,0.3] (HF), [13.3, 0.3] (CS), and [12.2, 1.5] (ISO).

HF states are further given in Sec. IV. The appearance of HF in a nematic liquid crystal is consistent with the conclusions drawn from Ref. [29] for a spherically confined system and from Ref. [31] for nematic liquid crystals in general.

Here we consider a single-chain problem ($n = 1$). A worm-like polymer is mathematically modeled by a continuous cylindrical filament; a contour variable s within the range $[0, L]$ is specified along the chain axial curve. The spatial position of a point on the curve at s is represented by the three-dimensional vector $\mathbf{r}(s)$. The unit vector $\mathbf{u}(s) = d\mathbf{r}/ds$ determines the tangent direction. The probability function for a chain configuration $\mathbf{r}(s)$ is assumed to be

$$\mathcal{P}[\mathbf{r}(s)] = \exp(-H_0 - H_{\text{int}}), \qquad (2)$$

where the reduced Hamiltonian

$$H_0 \equiv \frac{P}{2} \int_0^L ds \left(\frac{d\mathbf{u}}{ds}\right)^2 \qquad (3)$$

is the bending-energy penalty and

$$H_{\text{int}} = d \int_0^L ds \int_0^L ds' \delta[\mathbf{r}(s) - \mathbf{r}(s')]|\mathbf{u}(s) \times \mathbf{u}(s')| \qquad (4)$$

represents the excluded-volume interaction between the polymer segments at s and s' [30]. The DNA thread diameter d shows up here as the magnitude of the interaction.

The mathematical difficulty to analytically treat Eq. (2) is well known. The theoretical approach we took is the SCFT, which can be rigourously formulated and whose resulting differential equations can be precisely solved numerically. This powerful theoretical platform has had many successes in other structural-prediction problems in theoretical polymer physics [32–36]. The key step is to find the Green's function that represents the probability of a polymer segment which gives the segment distribution function $f(\mathbf{r}, \mathbf{u})$, that then can be used to describe the orientational distribution of segments along the direction specified by the unit vector $\mathbf{u}$, at a spatial location $\mathbf{r}$. In this paper we omit the entire theoretical derivation to arrive at the calculation of $f(\mathbf{r}, \mathbf{u})$, as it can be found in a review [37]; the main final equations to be solved are listed in Appendix A. The numerical solution yields different states corresponding to different branches of the free energy, which can be assessed from this theory. A comparison of the free energies allows us to identify a phase diagram in terms of two parameters, ρ_0 and P/R, discussed in Sec. III. Depending on

the length of the confined DNA (through ρ_0), the confinement dimension (P/R), and the shape of the confinement (fixed here to be spherical), the orientational field inside the confinement can display different states.

II. FOUR DISTINCT STRUCTURES

Here we describe the four types of confined states found on the basis of our numerical solutions of the distribution density to the wormlike-chain model, $f(\mathbf{r}, \mathbf{u})$. The solutions are computed at different values of $[\rho_0, P/R]$, and two branches sometimes coexist. Their main characteristics are illustrated in Fig. 1 by a number of visualization methods, some of which are defined in Appendix C.

Hopf fibrations (HF or CHF) are directionally ordered structures in the main body, which usually occur at high ρ_0. The local orientations of segments can be assessed from the Q-tensor calculated from $f(\mathbf{r}, \mathbf{u})$ [38]. Then, the nematic director $\mathbf{n}(\mathbf{r})$, to which most chain segments point, can be identified for each $\mathbf{r}$. The director view in the figure is presented by connecting the local nematic directors to form unit-vector fields. Following the red director curves in Figs. 1(a) and 1(d), for example, we can see that a red solenoid surface is formed on which the directors point in twisted directions continuously, resembling the texture on a French cruller. Layer by layer, from red, light grey, to light blue surfaces in Figs. 1(a) and 1(d), the director field varies continually until it converges to a central, circular solenoid axis inside the blue solenoid. The HF pattern was first proposed by Hopf [39] generally for directed vector fields and was previously seen in other fields of mathematics and physics. References [29,31] further describe the symmetry that the nematic director field $\mathbf{n}(\mathbf{r})$ must follow to form HF.

Our solution for the density distribution, $f(\mathbf{r}, \mathbf{u})$, enables the analysis that goes beyond the nematic-director view. Another representation of the directional ordering is the 3×3 tensor field $\mathbf{Q}(\mathbf{r})$, which is commonly used in liquid-crystal physics to measure the orientational ordering [38] and is defined in Appendix C together with the coloring methods used in an illustration. At a given spatial point $\mathbf{r}$, the Q-tensor can be diagonalize to yield three principal axes associated with the three main-axis eigenvalues. Then, the orientational properties can be described by plotting a three-dimensional ellipsoid specifying the main nematic direction and by defining a main-axis order parameter σ, taken from the three eigenvalues, that has the maximum magnitude. A needlelike shape indicates a strong orientational ordering (for which $\sigma \simeq 1$), a spherical-like shape denoting a directionally isotropic distribution ($\sigma \simeq 0$), and a pancakelike shape denoting an oblate distribution ($\sigma \simeq -1/2$). The left-hand panels of Figs. 1(b) and 1(e) contain these plots. In CHF, the chain segments in the central core region are directionally ordered in the vertical direction and in HF, disordered. This is further conceptually illustrated in the cross-section view of the director map, Figs. 1(a) and 1(d), where the yellow color represents the disordered region.

These visualization methods [and indeed our calculation of $f(\mathbf{r}, \mathbf{u})$] have the advantage of ignoring the effects of configurational fluctuations, hence precisely pinning down the ideal structures on average. This is particularly important

in studying the fundamental aspects of structural transitions where particle-based simulation methods are less effective. On the other hand, they do not directly show the actual chain configurations which have more visual impacts. Monte Carlo (MC) or molecular dynamics simulations deal with chain configurations on a more detailed molecular basis. For a wormlike chain confined in a spherical cavity, they were attempted in the past [16–24]. One of the technical challenges in these simulations is designing an algorithm that can efficiently bring the simulated systems to an equilibrium state under the extreme physical conditions known for the DNA confinement problem: slow simulation dynamics due to an extremely long chain, "jammed" configurations caused by the strong confinement, and the nature of the orientationally dependent excluded volume between cylindrical filaments. Some of the simulation difficulties can be more easily overcome for a similar confinement problem on short, multiple wormlike chains [40]. A recent molecular-dynamics simulation of a coarse-grained model provides concrete evidence that the HF configuration can be found by computer simulations as well [25]. HF was not found in Refs. [16–24].

We take an alternative MC approach here. From our SCFT calculation, we precisely determine an external mean field $W(\mathbf{r}, \mathbf{u})$ for a given state, which implicitly contains the excluded-volume information. The conformational properties of a long chain can then be simulated in a Monte Carlo simulation with $W(\mathbf{r}, \mathbf{u})$ in replacement of H_{int}. The method, known as the mean-field Monte Carlo (MFMC) method and clearly defined in Appendix D, approximates the actual chain configurations with some fluctuation effects. For illustration purposes, Figs. 1(c) and 1(f) are MFMC snapshots of HF and CHF; the texture formed by chain segments can be compared with the director map in Figs. 1(a) and 1(d). In particular, a careful examination of the central panels in Figs. 1(c) and 1(f) reveals the same orientational properties of the central panels of Figs. 1(a) and 1(d); vertical alignment of chain segments in the central core region can be observed in CHF but is not observed in HF. Section IV provides other physical measurements that demonstrate the differences between the two states.

At a lower ρ_0, the CS state is stable, illustrated by the director map in Fig. 1(g), displaying coaxial circles about the vertical axis in the outer layers; all local nematic directors are parallel to the latitude lines of the confining sphere. The yellow core region is less dense in chain segments, which are weakly ordered in the vertical direction; the MC configurations are further shown in Fig. 1(i). As the chain persistency increases, there is a strong competition between the packing requirement, which prefers the chain to make turns to reach the core region, and the DNA bending energy, which disfavors any sharp turns. This competition, together with the requirement of chain connectivity, has yielded some unique chain structures seen in recent computer simulations of packaging DNA [16,17,19,20,24]; on statistical average, the overall picture is consistent with the CS pattern.

At an even lower ρ_0, the isotropic (ISO) state is stable and it has a much simpler structure where the excluded-volume interactions do not dominate. Most segments in the central region have an isotropic orientational distribution, $\sigma \sim 0$; the
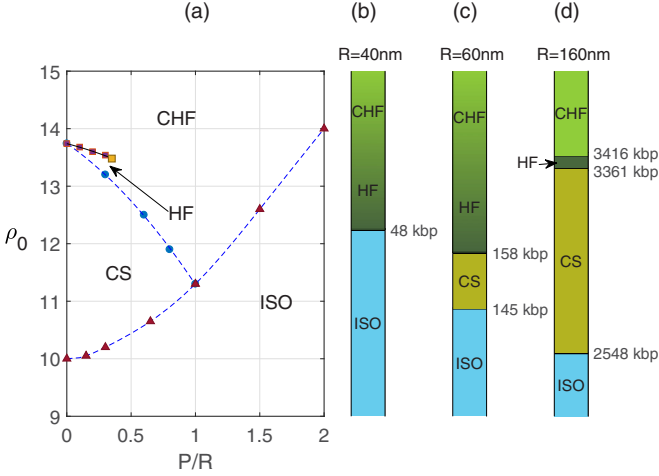
FIG. 2. Phase diagrams. (a) The calculated phase diagram in terms of the reduced density ρ_0 and P/R, based on SCFT. See Eq. (1) for the definition of ρ_0. The first-order phase transition is represented by solid black lines and second-order ones by dashed blue lines. The orange square is a critical point where the first-order line terminates. (b)–(d) Real examples produced from typical DNA parameters according to our theory (see Sec. III), where the smooth change of color in (b) and (c) represents crossovers.

only exception is near the confinement surface, where the DNA strands make typical tangential alignments with the wall surface, $\sigma \sim -1/2$, enforced by the steric interaction. In a tight confinement when $P/R \gtrsim 1$, the DNA strand winds around the interior of the confinement with no particular circling directions and creates a less dense regime in the center. The crossover of the conformational properties from weak confinement ($P/R \ll 1$) to strong confinement ($P/R \gg 1$) can be simply described by a ghost-chain model [41]. Richards *et al.* [2] referred to this DNA conformation as the ball model.

III. PHASE DIAGRAM

In which parameter regimes do we expect to see these states? Theoretically this is determined by the free-energy calculations, which are accessible through our work. In a few regimes, two solutions can coexist and the one corresponding to the lower free energy is deemed stable.

Figure 2(a) is a phase diagram in which ρ_0 defined in Eq. (1) and P/R are used as the basic parameters. The solid symbols are the actual phase boundaries determined from our numerical solutions and the curves are the interpolations to form the phase transition boundaries. The CS-ISO, CHF-ISO, and CS-HF phase transitions are second order and the HF-CHF transition is first order. The HF-CHF first-order transition terminates at a critical point at approximately $P/R = 0.35$, beyond which the parameter space is known as a supercritical region in thermodynamics.

The phase transitions occurring between the different states suggested here can have profound effects in DNA ejection [23]. In a confinement setting, the ratio P/R is fixed. The state of the confined DNA is controlled by nL/P (i.e., the number of confined base pairs) inside the cavity, through $\rho_0 = [(3/2\pi)(P/R)^3(d/P)](nL/P)$, where parameters in [$\cdots$] are all known. In ejection of a single confined DNA ($n = 1$), one

part of the confined DNA is released to the exterior space of the confinement [42–45]. As L/P decreases, a number of scenarios can happen. In strong confinement ($P/R \gtrsim 1$), the structure in the cavity undergoes a smooth crossover from CHF to HF, and then a phase transition to ISO; in intermediate confinement ($0.35 \lesssim P/R \lesssim 1$), the sequence is CHF-HF, HF-CS, and CS-ISO, where CHF-HF is a smooth crossover; and in weak confinement ($P/R \lesssim 0.35$), the phase-transition sequence is CHF-HF, HF-CS, and CS-ISO. Although DNA ejection is a dynamic process, as L/P inside the cavity is reduced across the phase boundaries in Fig. 2, the thermodynamics of the interior DNA portion requires structural reorganization in order to make transitions to the new states. This has a direct impact on the released DNA portion in the exterior; indeed, the observed curve of released DNA length versus releasing time from a bacteriophage is known to have two or three kinks [42,45]. A plausible explanation is that these kinks correspond to the phase transitions occurring in the confined DNA portion.

The phase diagram is presented here in reduced units. To place it in the perspective of real systems, we present here a few examples. Typical DNA length scales, $d = 2$ nm, $P = 50$ nm [46–49], and 1 kb = 0.34 μm are adopted. Then, the conversion $\rho_0 = 16000L/R^3$ can be established where the units for L and R are kilobase and nanometers, respectively. Taking $R = 40$ nm (T5 phage in Ref. [43]), we illustrate a one-dimensional phase diagram, presented in Fig. 2(b), divided into two regions according to L. Whereas in another scenario, if we let $R = 60$ nm, the one-dimensional phase diagram in Fig. 2(c) covers three different regions. In a weak confinement case, $R = 160$ nm, the CHF-HF crossover in Fig. 2(c) is now a clear phase transition.

The theoretical phase diagram in Fig. 2 can be used as a reference for real systems, but the precise location of these boundaries could shift because of parameter identification; in particular, most real confinement geometries are not perfectly spherical. In addition, it is known, for example, that the Onsager treatment of the directionally dependent excluded-volume interactions marginally underestimates the liquid-crystal transition density in comparison with real systems. This can be traced back to the second-virial approximation taken by Onsager [30].

On the surface layer, HF and CHF can be easily related to a helical pattern. The tilt angle that the nematic director makes with respect to the equator latitude at the surface, γ, becomes a characteristic measure for the apparent helical pattern. Kosturko *et al.* [5] reported that the surface DNA layer indeed demonstrates a helical pattern, which provides indirect experimental evidence of the existence of HF structures. A close biological system is DNA condensates that form a toroid; it is known that DNA winds the toroidal axis layer by layer with varying twist angles [50]. Experimentally, the CS-HF-CHF transition sequence ought to be measurable by observing the tilt angle γ, which jumps from zero (CS) to a finite value (HF), and then to another larger value (CHF), on the outermost-shell image of the confined DNA.

Shin and Grason took the Frank-energy model as the starting point of a theoretical model for DNA packing in spherical confinement [29]. The model was written in terms of the deformation of the nematic director field and contains λ/R,

K_3/K, and K_2/K as the three phenomenological parameters where λ is related to K, and K, K_2, and K_3 are the Frank deformation modulus in the one-constant approximation, and bending and twisting moduli of a solenoid texture. They showed that a sequence of three topologically different states is possible: CS, twisted solenoid (similar to our HF), and simple solenoid (an extreme case of our CHF when $\gamma = \pi/2$). As K_3/K increases, they found that the system undergoes a phase-transition sequence of CS to twisted solenoid, and then twisted to simple solenoids. This is similar to our phase diagram with a small fixed P/R, where the packed wormlike chain undergoes the CS-HF-CHF sequence of phase transitions, as the overall packed DNA density ρ_0 increases. There is no consideration of the density variation in Frank energy. No connection between the Frank elastic moduli and the physical parameters $[\rho_0, P/R]$ used here can be found in the current literature.

Finally, we comment on the ISO phase boundary by taking a horizontal path on the phase diagram for a fixed ρ_0. Generally, the naive picture of confinement in an entropy-driven soft matter system is to induce ordering. In contrast, the current system has a competing bending energy of the polymer, which dominates over the entropy of the bulk region at a large P/R. Most polymer segments are pushed towards the surface shell. Now, the entropy of winding the shell region in an arbitrary direction (in an ISO state) prevails over the azimuthal ordering (in a CS or HF state). This is responsible for the CS-ISO transition, or HF-ISO transition when P/R increases with a fixed ρ_0.

IV. HF-CHF TRANSITION

In this section, we clarify a subtle issue: How different are the two Hopf fibration states, HF and CHF? They depend on the ratio P/R and may appear to occupy a small range in the phase diagram (Fig. 2); however, when R/P (instead of P/R) is used as the horizontal axis, the transition region is significant. Figures 3(a) and 3(b) display two different scenarios as we change ρ_0 for two prototypical values of $P/R = 0.3$ and 2.0, respectively. One common feature is that the director maps of CHF in Figs. 3(a) and 3(b) (far right) have two defect "points" (yellow) near the north and south poles where the orientational order parameter vanishes.

A small P/R system feels fewer wall effects and as such the density distribution profile in the bulk is more uniform. Below $\rho_0 \lesssim 13$, the orientational entropy dominates and hence the bulk state is isotropic. Above $\rho_0 \gtrsim 14$, the Onsager interaction dominates and hence the bulk state is nematic. The existence of such a first-order isotropic-nematic phase transition was well documented in the literature for the bulk state [51–54]. In the case $P/R = 0.3$, this manifests in the form of a first-order HF-CHF transition at $\rho_0 = 13.54$. The qualitative picture was suggested in Refs. [41,55]. At this transition point, as illustrated in Fig. 3, the density profile [in Fig. 3(a)], the overall liquid-crystal order parameter σ [in Fig. 3(c)], and the tilt angle γ [in Fig. 3(d)] all change abruptly. The physical mechanism is similar to the partial-wetting to complete-wetting transition of wormlike chains confined between two parallel plates, found by solving the wormlike-chain model [56,57] and MC simulations [58–61].
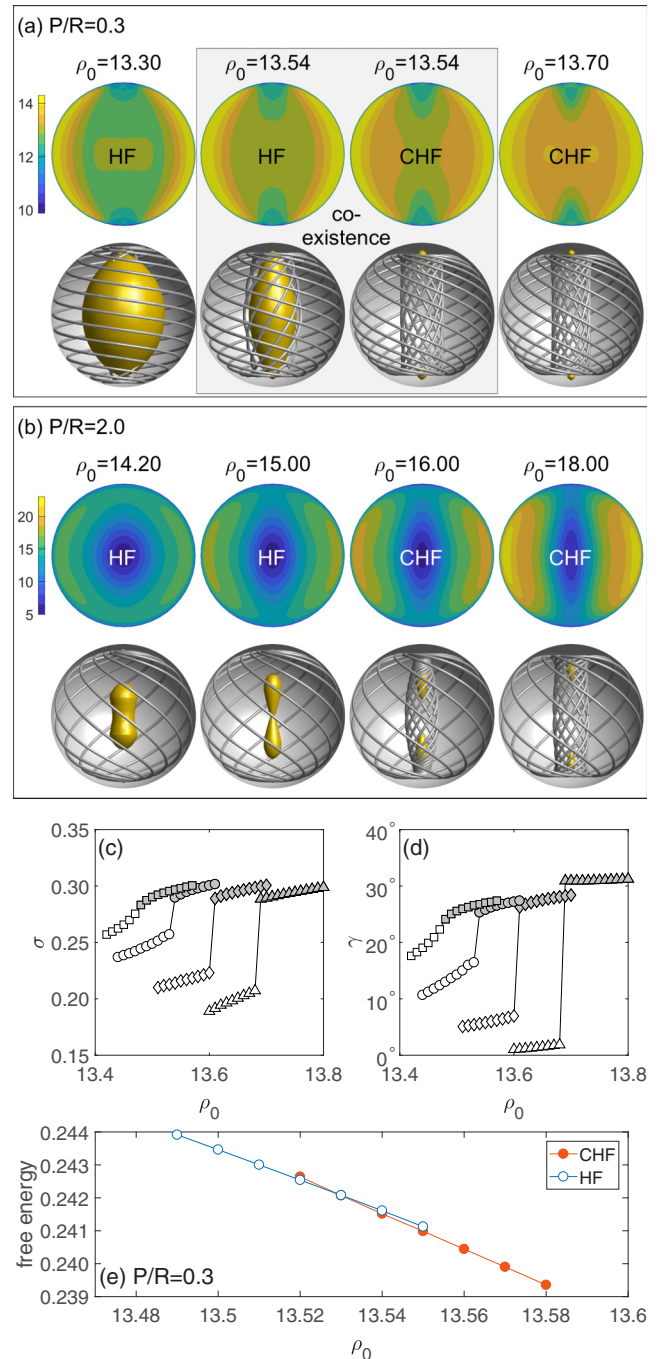

FIG. 3. HF-CHF structural transition and crossover. The density profiles and director maps in (a) are displayed for the first-order HF-CHF transition as the overall DNA density ρ_0 increases inside the spherical cavity for $P/R = 0.3$; in contrast, the density profiles and director maps in (b) are a smooth HF-CHF crossover as ρ_0 changes at $P/R = 2.0$. This can be further assessed by the changes in (c) the mean order parameter σ and (d) the tilt angle γ across the HF-CHF transition, for $P/R = 0.1$ (triangles), 0.2 (diamonds), 0.3 (circles), and 0.35 (squares). (e) The reduced free energies of HF and CHF as functions of ρ_0 for $P/R = 0.3$.

In stronger confinement, $P/R > 0.35$, however, the bending of DNA inside the cavity to accommodate both confinement constraint and single-chain continuity creates a density depletion near the spherical center, as demonstrated in

Fig. 3(b). The very mechanism that leads to the HF-CHF phase transition now disappears. The single central isotropic core smoothly transits into two isotropic regions, and then subsequently to two points in the north and south poles. There is no phase transition here. $P/R \simeq 0.35$ is then a critical point that separates this "supercritical" behavior from the first-order transition region.

Figure 3(c) and 3(d) are plots for the mean order parameter σ and tilde angle γ for fixed P/R as ρ_0 varies. The solid and open symbols represent CHF and HF states, respectively. At the first-order transitions below $P/R \leqslant 0.35$, the gaps on these curves are clearly visible. Once the critical point $P/R \approx 0.35$ is approached, the gaps close. This can be compared to a typical liquid-gas transition phase diagram near its critical point. Figure 3(e) displays the free energies, reduced by a factor of $2P\beta/L$, of the HF and CHF branches at $P/R = 0.3$, which clearly shows how they cross each other at the transition density. Away from the transition density, the free energy difference is apparently small; however, a 0.1% change in ρ_0 approximately corresponds to a 0.1% change in the free energy, which is significant.

V. CONCLUDING REMARKS

The SCFT calculation in this paper forms a firm theoretical foundation for interpretation of the structural properties of DNA in spherical-like confinement. Most recent experimental and simulation results are built on a spooling concept [3–5,8,10–12,14,27,28,62]; our understanding of the phase transitions between the three orientationally ordered states, CHF, HF, and CS, yields the promise to further understand DNA confinement in fine detail and to shed light on the DNA ejection dynamics [22,23,42–45].

Here are additional remarks on the validity of our approach and the applicability of the main results.

(1) In order to compare with the DNA confinement problem, we take the limit $L/P \gg 1$ in our calculation for a single confined polymer ($n = 1$). We can show that the main SCFT results calculated in this work formally remain the same for multiple long polymer chains ($L/P \gg 1$ and $n \neq 1$), as long as ρ_0 is used as a reduced parameter, of course, with a factor n seen in Eq. (1). This is because the dominating physics is the excluded-volume interaction between polymer segments, produced regardless of either intra- or interchain interactions; the long-chain limit guarantees that the polymer end effects are not important. Our SCFT approach is enabled by such a physical picture.

(2) The problem of multiple wormlike polymers confined in a spherical cavity can take another form, closer to confined liquid-crystal polymers, when L/P is *finite*. For these systems, the bipolar, twisted bipolar [63], and tennis-ball structures [40,64,65] are now known to be stable. Although this problem is not our main concern here, we point out that by keeping L/P finite in our theory, the basic SCFT framework can be used to model these states as well. Essentially, we would be required to calculate the orientationally order structures in a three-dimensional parameter space $[\rho_0, P/R, L/P]$ instead of the two-dimensional parameter space $[\rho_0, P/R, L/P \gg 1]$ presented in this work. From this angle, we also expect that the SCFT builds a bridge between the classical DNA confinement

problem and the vast theoretical and simulation literature of liquid crystals confined in a spherical cavity, reported in recent years.

(3) The same SCFT formalism is adaptive for describing other liquid-crystal and polymer problems. Taking $L/P \ll 1$, we examined rigid liquid-crystal molecules confined on a spherical surface [66,67] and on a flat surface with line boundaries [68,69] where the geometry frustrations produce nematic defect patterns. Taking $L/P \gg 1$, we calculated the conformational properties of DNA molecules strongly confined in a tube [70–72] where the wormlike-chain model produces a richer scaling behavior than the Gaussian-chain model. Using L/P as a varying parameter, we predicted the phase diagrams for liquid-crystal polymers confined between parallel plates and on a toroidal surface [57,73] where the polymer persistency plays a role in stabilizing orientationally ordered states.

(4) The wormlike-chain model uses d and P as the basic theoretical parameters. The electrostatic repulsion with screening can be effectively accounted for within a self-avoiding wormlike-chain model, but now d and P must be regarded as effective and "dressed" system parameters, which can change according to the ionic strength of the solvent. We refer to a scholarly review on how the effective d and P can be used for such a case [52].

(5) A viral capsid that packs DNA is known to have different confinement shapes (e.g., icosahedral) and may contain other biological features in the interior. Here we used a "spherical cow"-type model to represent the overall confinement by a perfect sphere, as a first attempt to understand the confinement problem. The inclusion of the biological details may change the symmetry of the particular phases discovered in this work. However, we expect that the general physical picture, that this confined system undergoes multiple stages of phase transitions in the vicinity of ρ_0 indicated in our phase diagram, still stands.

(6) The current study is based on a field description, and the particle-level spatial resolution is completely smoothed out within the spherical interior. Some experimental results, however, show explicit packing layering with fine spatial resolution at the scale of DNA width d. The current approach cannot describe such layering.

APPENDIX A: SELF-CONSISTENT FIELD THEORY

In this work, we use the wormlike-chain model to represent the configurations of DNA. The basic model is described by the Boltzmann weight, Eq. (2), which is written in terms of a phantom-chain Hamiltonian, Eq. (3), and an interaction Hamiltonian, Eq. (4). Solving the problem exactly is prohibitive because of the difficulties associated with handling H_{int}. The SCFT is a conventional and successful theoretical

procedure used in treating polymer statistics with segment-segment interactions, as documented in Refs. [32–36,74–77]. The particular version we used here for the wormlike-chain model in the above can be found in a review [37], step by step. The basic assumptions and derivations made in the current approach are laid out in this Appendix.

A long polymer chain is considered (i.e., $L \gg P$), which winds itself inside the cavity. As such, a segment interacts with another segment through H_{int}. Effectively, to consider a single-chain partition function, the excluded-volume interaction from other portions of the chain is replaced by a background, self-consistent field $W(\mathbf{r}, \mathbf{u})$. The reduced Hamiltonian is

$$H_{scf} = \frac{1}{2P} \int_0^L \mathrm{d}s W[\mathbf{r}(s), \mathbf{u}(s)]. \qquad (A1)$$

Note that a $2P$ factor (the effective Kuhn length) is included to keep W dimensionless.

The total reduced Hamiltonian is then rewritten as, at this stage in an exact form,

$$H = H_0 + H_{int} = [H_0 + H_{scf}] + [H_{int} - H_{scf}]. \qquad (A2)$$

The Hamiltonian in the first set of brackets is considered below for the calculation of the partition function Q by taking into account all possible polymer configurations; as an approximation, the Hamiltonian in the second set of brackets is treated at the free-energy level with replacement of the fluctuating quantities by their averages. Therefore, the total reduced free energy is

$$\beta F = -\ln Q + \frac{dL^2}{V^2} \int \mathrm{d}\mathbf{r}\mathrm{d}\mathbf{u}\mathrm{d}\mathbf{u}' |\mathbf{u} \times \mathbf{u}'| f(\mathbf{r}, \mathbf{u}) f(\mathbf{r}, \mathbf{u}')$$
$$- \frac{L}{2PV} \int \mathrm{d}\mathbf{r}\mathrm{d}\mathbf{u} W(\mathbf{r}, \mathbf{u}) f(\mathbf{r}, \mathbf{u}). \qquad (A3)$$

The mean density function

$$f(\mathbf{r}, \mathbf{u}) = \left\langle \frac{V}{L} \int_0^L \mathrm{d}s \delta[\mathbf{r} - \mathbf{r}(s)] \delta[\mathbf{u} - \mathbf{u}(s)] \right\rangle \qquad (A4)$$

is introduced here, which is obtained from the configurational average $\langle \cdots \rangle$ performed according to the Hamiltonian in the first set of brackets. Note that f is normalized,

$$\int \mathrm{d}\mathbf{r}\mathrm{d}\mathbf{u} f(\mathbf{r}, \mathbf{u}) = V, \qquad (A5)$$

where $V = 4\pi R^3/3$ is the volume. The free-energy functional is minimized with respect to W and f to determine various quantities self-consistently. The minimization with respect to the density $f(\mathbf{r}, \mathbf{u})$ leads to

$$W(\mathbf{r}, \mathbf{u}) = 2\rho_0 \int d\mathbf{u}' f(\mathbf{r}, \mathbf{u}') |\mathbf{u} \times \mathbf{u}'|. \qquad (A6)$$

Hence W is self-consistently determined by the distribution function itself.

The logic behind the SCFT concept outlined here can be more rigorously established (but is more mathematically involved) by the use of the Hubbard-Stratonovich transformation, which is a general approach taken in the particle-picture-to-field-picture transformation, and by the saddle-point approximation, which is commonly used to select the optimal

W profile of the transformed field. For a general procedure of establishing the SCFT of a system composed of Gaussian polymers, one can refer to Refs. [32,36,74]; for wormlike polymers, Ref. [37].

The calculation of the partition function requires the performance of integration over all polymer configurations:

$$Q \propto \int D[\mathbf{r}(s)]D[\mathbf{u}(s)] \exp[-H_0 - H_{scf}]. \qquad (A7)$$

The integration can be equivalently mapped into solving a modified diffusion equation (MDE). For this purpose, a polymer segment of contour length s is considered and its s terminal is assumed to appear at the location specified by the coordinate vector $\mathbf{r}$ and to point at the direction specified by the unit vector $\mathbf{u}$. The probability of finding such a segment, $q(\mathbf{r}, \mathbf{u}; s)$ (a propagator), is based on a two-point Green's function with the variables associated with the $s = 0$ end integrated out. It satisfies

$$\frac{\partial}{\partial s} q = \left[\frac{1}{2P} \nabla_{\mathbf{u}}^2 - \mathbf{u} \cdot \nabla_{\mathbf{r}} \Big|_{\mathbf{u}} - \frac{1}{2P} W(\mathbf{r}, \mathbf{u}) \right] q. \qquad (A8)$$

Though this MDE was formulated before [78], a careful derivation is given in Ref. [79] for non-Cartesian frames, where special attention is paid to the meaning of the spatial gradient term.

In the long-chain limit, which is the main concern of the current work, the so-called ground-state dominance "approximation" is a useful theoretical tool and is asymptotically *exact* [80]. In most cases, the physical properties are s independent and hence the s dependence can be removed. The propagator can now be written as

$$q(\mathbf{r}, \mathbf{u}; s) = \exp(-\mu s/2P) q'(\mathbf{r}, \mathbf{u}), \qquad (A9)$$

where μ is the ground-state eigenvalue of the equation,

$$\mu q'(\mathbf{r}, \mathbf{u}) = \left[W(\mathbf{r}, \mathbf{u}) + 2P\mathbf{u} \cdot \nabla_{\mathbf{r}} - \nabla_{\mathbf{u}}^2 \right] q'(\mathbf{r}, \mathbf{u}), \qquad (A10)$$

which is solved in the current work instead of solving Eq. (A8). The partition function is given by

$$-\ln Q = \mu L/2P, \qquad (A11)$$

and the distribution function is

$$f(\mathbf{r}, \mathbf{u}) = C^{-1} q'(\mathbf{r}, \mathbf{u}) q'(\mathbf{r}, -\mathbf{u}). \qquad (A12)$$

In the rest of this paper, the prime on q is dropped, with the understanding that the above relationships are adopted. Here $C = V^{-1} \int \mathrm{d}\mathbf{r}\mathrm{d}\mathbf{u} q(\mathbf{r}, \mathbf{u}) q(\mathbf{r}, -\mathbf{u})$ is a normalization factor, with V being the volume of the sphere.

The entire theory contains ρ_0 as the reduced density introduced in Eq. (1) of the text. Note that there are only *two* system-dependent parameters in this theory: ρ_0 and P/R. The latter shows up in the second term on the right-hand side of Eq. (A10), after rescaling $\mathbf{r}$ by R.

APPENDIX B: NUMERICAL COMPUTATION

In brief summary, to perform a calculation for the current problem, for a field W, the MDE (A10) needs to be solved for q. The density profile is then produced from Eq. (A12) and through Eq. (A6) gives W. Looping through these self-consistent steps yields a solution for the problem. The free-

energy is evaluated from

$$2P\frac{\beta F}{L} = \frac{1}{V}\left[\rho_0 \int d\mathbf{r} \int d\mathbf{u} \int d\mathbf{u}' f(\mathbf{r}, \mathbf{u}) f(\mathbf{r}, \mathbf{u}') |\mathbf{u} \times \mathbf{u}'|\right.$$
$$\left. - \int d\mathbf{r} \int d\mathbf{u} W(\mathbf{r}, \mathbf{u}) f(\mathbf{r}, \mathbf{u})\right] + \mu \qquad \text{(B1)}$$

for assessing the stability of a state and for producing the phase diagram in the text.

The numerical solution of the eigenproblem in Eq. (A10) requires the consideration of the propagator q as a function of five variables: three components for $\mathbf{r}$ and two components for $\mathbf{u}$. The variable space can be reduced if a certain symmetry is expected. Here we found that by simply discretizing the q function in the five-dimensional space, with implementation of parallel computation, enables us to calculate the propagator efficiently. A typical solution for a given $[\rho_0, P/R]$ point, carried out on 32 processors, takes approximately a few hours.

We initially used a numerical guess for the simplest ISO state. As we scan the phase diagram in Fig. 2 by increasing ρ_0 with fixed P/R, the ISO solution bifurcates at the ISO-CS and ISO-HF boundaries. At a relatively large P/R, HF smoothly crosses over to CHF. Once these four states were discovered, we took multiple paths to scan the phase diagram, to ensure that all regions are covered. This time, to produce a solution for a particular state (HF, CHF, CS, or ISO) at given $[\rho_0, P/R]$, an initial guess was taken from an existing solution of that state at a neighboring point of $[\rho_0, P/R]$.

APPENDIX C: VISUALIZATION FOR ORIENTATIONAL ORDERING

We solved the model in the last section by using a spherical coordinate system [41,55,79]. An important result is $f(\mathbf{r}, \mathbf{u})$, which is the probability density of finding a chain segment at a spatial position specified by the vector $\mathbf{r}$ and pointing at the direction specified by the unit vector $\mathbf{u}$. The numerical solutions to SCFT yield the distribution functions $f(\mathbf{r}, \mathbf{u})$ precisely for the four states discussed in the paper.

The density profile plotted on the right-hand panels of Figs. 1(b), 1(e), 1(h), 1(k), 3(a), and 3(b) is calculated from

$$\rho(\mathbf{r}) = \rho_0 \int d\mathbf{u} f(\mathbf{r}, \mathbf{u}). \qquad \text{(C1)}$$

Following the convention used in the liquid-crystal theory, the local orientational distribution at $\mathbf{u}$ is characterized by

computing the 3×3 tensor $\mathsf{Q}(\mathbf{r})$ which contains the elements calculated from [38],

$$Q_{ij}(\mathbf{r}) = \frac{\int d\mathbf{u}(3u_i u_j - \delta_{ij}) f(\mathbf{r}, \mathbf{u})}{2 \int d\mathbf{u} f(\mathbf{r}, \mathbf{u})}, \qquad \text{(C2)}$$

where u_i ($i = x, y, z$) is the ith Cartesian component of $\mathbf{u}$. Based on this traceless tensor, three eigenvalues are then obtained, $\lambda_1 \geqslant \lambda_2 \geqslant \lambda_3$. Hence the orientational property can be represented by an ellipsoid with axes $a_i = \lambda_i + 1/2$, where $i = 1, 2, 3$. As the result, an idealized, needlelike distribution is illustrated by ellipsoid with $a_1 = 3/2$, $a_2 = a_3 = 0$. An isotropic state is illustrated by a sphere with all $a_i = 1/2$. A pancakelike distribution is illustrated by an oblate with $a_1 = a_2 = 3/4$, $a_3 = 0$. This method is used in producing the left-hand panels of Figs. 1(b), 1(e), 1(h), and 1(k). The eigenvector corresponding to λ_1 is used as the local director in Figs. 1(a), 1(d), and 1(g).

In Fig. 1, we also use color to represent the orientational ordering. An order parameter $\sigma(\mathbf{r})$ is defined from the eigenvalues, $\sigma(\mathbf{r}) = \lambda_1$ if $|\lambda_1| > |\lambda_3|$ and $\sigma(\mathbf{r}) = \lambda_3$ otherwise. Then, a needlelike distribution has $\sigma = 1$ and an oblate distribution $\sigma = -1/2$. The isotropic distribution is represented by $\sigma = 0$. A color map can then be produced for σ.

APPENDIX D: MEAN-FIELD MONTE CARLO

One can show that the probability density produced from solving Eq. (A10) self-consistently is equivalent to an effective wormlike-chain model for a single chain, with the chain statistics satisfying the probability

$$\mathcal{P} = \exp\left\{-H_0 - \frac{1}{2P} \int_0^L W[\mathbf{r}(s), \mathbf{u}(s)] ds\right\}.$$

Note that there is no intrachain interaction anymore, as it is now effectively represented by $W[\mathbf{r}(s), \mathbf{u}(s)]$, the self-consistent field.

This offers the opportunity to conduct a single-chain Monte Carlo simulation *without* including the interaction Hamiltonian in Eq. (4). The continuum version assumes a continuous function $\mathbf{r}(s)$, which can be represented by a discrete chain connected by bonds of small length Δs. Hence, after solving the SCFT to obtain W, one can conduct Monte Carlo simulations on a discrete chain following this weight to reproduce typical segmental coordinates for each given type of $W(\mathbf{r}, \mathbf{u})$ (HF, CHF, CS, and ISO), inside the confinement sphere of radius R.

[1] S. Klimenko, T. Tikchonenko, and V. Andreev, J. Mol. Biol. **23**, 523 (1967).

[2] K. Richards, R. Williams, and R. Calendar, J. Mol. Biol. **78**, 255 (1973).

[3] W. C. Earnshaw and S. C. Harrison, Nature (London) **268**, 598 (1977).

[4] W. C. Earnshaw, J. King, S. C. Harrison, and F. A. Eiserling, Cell **14**, 559 (1978).

[5] L. Kosturko, M. Hogan, and N. Dattagupta, Cell **16**, 515 (1979).

[6] Y. Fujiyoshi, H. Yamagishi, T. Kunisada, H. Sugisaki, T. Kobayashi, and N. Uyeda, J. Ultrastruct. Res. **79**, 235 (1982).

[7] L. W. Black, W. W. Newcomb, J. W. Boring, and J. C. Brown, Proc. Natl. Acad. Sci. USA **82**, 7960 (1985).

[8] J. Lepault, J. Dubochet, W. Baschong, and E. Kellenberger, EMBO J. **6**, 1507 (1987).

[9] N. V. Hud, Biophys. J. **69**, 1355 (1995).

[10] M. E. Cerritelli, N. Q. Cheng, A. H. Rosenberg, C. E. McPherson, F. P. Booy, and A. C. Steven, Cell **91**, 271 (1997).

[11] Z. Zhang, B. Greene, P. A. Thuman-Commike, J. Jakana, P. E. Prevelige, Jr., J. King, and W. Chiu, J. Mol. Biol. **297**, 615 (2000).

[12] A. Fokine, P. R. Chipman, P. G. Leiman, V. V. Mesyanzhinov, V. B. Rao, and M. G. Rossmann, Proc. Natl. Acad. Sci. USA **101**, 6003 (2004).

[13] A. Kato, E. Shindo, T. Sakaue, A. Tsuji, and K. Yoshikawa, Biophys. J. **97**, 1678 (2009).

[14] L. R. Comolli, A. J. Spakowitz, C. E. Siegerist, P. J. Jardine, S. Grimes, D. L. Anderson, C. Bustamante, and K. H. Downing, Virology **371**, 267 (2008).

[15] M. Negishi, T. Sakaue, K. Takiguchi, and K. Yoshikawa, Phy. Rev. E **81**, 051921 (2010).

[16] J. Kindt, S. Tzlil, A. Ben-Shaul, and W. M. Gelbart, Proc. Natl. Acad. Sci. USA **98**, 13671 (2001).

[17] J. Arsuaga, R. K. Z. Tan, M. Vazquez, D. W. Sumners, and S. C. Harvey, Biophys. Chem. **101–102**, 475 (2002).

[18] E. Katzav, M. Adda-Bedia, and A. Boudaoud, Proc. Natl. Acad. Sci. USA **103**, 18900 (2006).

[19] A. S. Petrov, M. B. Boz, and S. C. Harvey, J. Struct. Biol. **160**, 241 (2007).

[20] C. R. Locker, S. D. Fuller, and S. C. Harvey, Biophys. J. **93**, 2861 (2007).

[21] S. C. Harvey, A. S. Petrov, B. Devkota, and M. B. Boz, in *Methods in Enzymology*, edited by M. L. Johnson and L. Brand (Academic Press, New York, 2011), Vol. 487, pp. 513–543.

[22] D. Reith, P. Cifra, A. Stasiak, and P. Virnau, Nucleic Acids Res. **40**, 5129 (2012).

[23] D. Marenduzzo, C. Micheletti, E. Orlandini, and W. de Sumners, Proc. Natl. Acad. Sci. USA **110**, 20081 (2013).

[24] D. C. Rapaport, Phys. Rev. E **94**, 030401(R) (2016).

[25] T. Curk, J. D. Farrell, J. Dobnikar, and R. Podgornik, Phys. Rev. Lett. **123**, 047801 (2019).

[26] S. C. Harrison, J. Mol. Biol. **171**, 577 (1983).

[27] A. Minsky, E. Shimoni, and D. Frenkiel-Krispin, Nat. Rev. Mol. Cell Biol. **3**, 50 (2002).

[28] J. E. Johnson and W. Chiu, Curr. Opin. Struct. Biol. **17**, 237 (2007).

[29] H. Shin and G. M. Grason, Europhys. Lett. **96**, 36007 (2011).

[30] L. Onsager, Ann. N. Y. Acad. Sci. **51**, 627 (1949).

[31] B. G.-g. Chen, P. J. Ackerman, G. P. Alexander, R. D. Kamien, and I. I. Smalyukh, Phys. Rev. Lett. **110**, 237801 (2013).

[32] G. Fredrickson, *The Equilibrium Theory of Inhomogeneous Polymers* (Oxford University Press, New York, 2006), Vol. 134.

[33] E. Helfand, J. Chem. Phys. **62**, 999 (1975).

[34] M. Whitmore and J. Vavasour, Acta Polym. **46**, 341 (1995).

[35] T. A. Vilgis, Phys. Rep. **336**, 167 (2000).

[36] M. W. Matsen, J. Phys.: Condens. Matter **14**, R21 (2001).

[37] J. Z. Y. Chen, Prog. Polym. Sci. **54–55**, 3 (2016).

[38] P. G. De Gennes and J. Prost, *The Physics of Liquid Crystals*, 2nd ed. (Clarendon Press, Oxford, UK, 1993).

[39] H. Hopf, Math. Ann. **104**, 637 (1931).

[40] A. Nikoubashman, D. A. Vega, K. Binder, and A. Milchev, Phys. Rev. Lett. **118**, 217803 (2017).

[41] J. Gao, P. Tang, Y. Yang, and J. Z. Y. Chen, Soft Matter **10**, 4674 (2014).

[42] N. Chiaruttini, M. De Frutos, E. Augarde, P. Boulanger, L. Letellier, and V. Viasnoff, Biophys. J. **99**, 447 (2010).

[43] M. D. Frutos, A. Leforestier, and F. Livolant, Biophys. Rev. Lett. **09**, 81 (2014).

[44] C. M. Knobler and W. M. Gelbart, Annu. Rev. Phys. Chem. **60**, 367 (2009).

[45] A. Evilevitch, eLife **7**, e37345 (2018).

[46] C. Bustamante, J. F. Marko, E. D. Siggia, and S. Smith, Science **265**, 1599 (1994).

[47] J. F. Marko and E. D. Siggia, Macromolecules **28**, 8759 (1995).

[48] T. E. Cloutier and J. Widom, Mol. Cell **14**, 355 (2004).

[49] P. Gross, N. Laurens, L. B. Oddershede, U. Bockelmann, E. J. Peterman, and G. J. Wuite, Nat. Phys. **7**, 731 (2011).

[50] N. V. Hud, K. H. Downing, and R. Balhorn, Proc. Natl. Acad. Sci. USA **92**, 3581 (1995).

[51] A. Khokhlov and A. Semenov, Phys. A **112**, 605 (1982).

[52] T. Odijk, Macromolecules **19**, 2313 (1986).

[53] G. J. Vroege and T. Odijk, Macromolecules **21**, 2848 (1988).

[54] Z. Y. Chen, Macromolecules **26**, 3419 (1993).

[55] N. N. Oskolkov, P. Linse, I. I. Potemkin, and A. R. Khokhlov, J. Phys. Chem. B **115**, 422 (2011).

[56] J. Z. Y. Chen, D. E. Sullivan, and X. Yuan, Macromolecules **40**, 1187 (2007).

[57] S. Ye, P. Zhang, and J. Z. Y. Chen, Soft Matter **12**, 2948 (2016).

[58] V. A. Ivanov, A. S. Rodionova, E. A. An, J. A. Martemyanova, M. R. Stukan, M. Müller, W. Paul, and K. Binder, Phys. Rev. E **84**, 041810 (2011).

[59] A. V. Emelyanenko, S. Aya, Y. Sasaki, F. Araoka, K. Ema, K. Ishikawa, and H. Takezoe, Phys. Rev. E **84**, 041701 (2011).

[60] V. A. Ivanov, A. S. Rodionova, J. A. Martemyanova, M. R. Stukan, M. Müller, W. Paul, and K. Binder, J. Chem. Phys. **138**, 234903 (2013).

[61] V. A. Ivanov, A. S. Rodionova, J. A. Martemyanova, M. R. Stukan, M. Müller, W. Paul, and K. Binder, Macromolecules **47**, 1206 (2014).

[62] N. V. Hud and I. D. Vilfan, Annu. Rev. Biophys. Biomol. Struct. **34**, 295 (2005).

[63] R. D. Williams, J. Phys. A: Math. Gen. **19**, 3211 (1986).

[64] Y. Hu, Y. Qu, and P. Zhang, Commun. Comput. Phys. **19**, 354 (2016).

[65] Y. Qu, Y. Wei, and P. Zhang, Commun. Comput. Phys. **21**, 890 (2017).

[66] W.-Y. Zhang, Y. Jiang, and J. Z. Y. Chen, Phys. Rev. Lett. **108**, 057801 (2012).

[67] Q. Liang, S. Ye, P. Zhang, and J. Z. Y. Chen, J. Chem. Phys. **141**, 244901 (2014).

[68] J. Z. Y. Chen, Soft Matter **9**, 10921 (2013).

[69] X. Yao, H. Zhang, and J. Z. Y. Chen, Phys. Rev. E **97**, 052707 (2018).

[70] J. Z. Y. Chen, Macromolecules **46**, 9837 (2013).

[71] J. Z. Y. Chen, Phys. Rev. Lett. **118**, 247802 (2017).

[72] J. Z. Y. Chen, Phys. Rev. Lett. **121**, 037801 (2018).

[73] S. Ye, P. Zhang, and J. Z. Y. Chen, Soft Matter **12**, 5438 (2016).

[74] M. Müller and F. Schmid, in *Advanced Computer Simulation Approaches for Soft Matter Sciences II* (Springer, Berlin, 2005), pp. 1–58.

[75] G. H. Fredrickson, V. Ganesan, and F. Drolet, Macromolecules **35**, 16 (2002).

[76] A.-C. Shi, *Encyclopedia of Polymeric Nanomaterials*, edited by S. Kobayashi and K. Müllen (Springer, Berlin, 2015).

[77] I. W. Hamley, *Developments in Block Copolymer Science and Technology* (Wiley, New York, 2004).

[78] K. F. Freed, Adv. Chem. Phys. **22**, 1 (1972).

[79] Q. Liang, J. Li, P. Zhang, and J. Z. Y. Chen, J. Chem. Phys. **138**, 244910 (2013).

[80] A. Y. Grosberg, A. R. Khokhlov, and Y. A. Atanov, *Statistical Physics of Macromolecules* (AIP, New York, 1994).